# Lyapunov-Based Control Strategy for a Single-Input Dual-Output Three-Level DC/DC Converter

Milad Rasouli, Majid Mehrasa, Amir Ganjavi, Mahdieh S. Sadabadi, Hoda Ghoreishy and Ahmad Ale Ahmad

***Abstract*—This paper proposes a robust control strategy using direct Lyapunov strategy (DLS) for a single-input dual-output three-level dc-dc converter (SIDO-TLC) while the output loads and voltage references are disturbed. The first proceeding is to concurrently focus on the current and voltage dynamics of the converter buck and boost segments for exerting the related variable errors to the DLS-based function. Accordingly, through a comprehensive analysis based on the outcome of this proceeding, the PI controller coefficients allotted to the current reference design process are enabled to reach their maximum robustness capabilities against any output voltage variation. Moreover, the converter reference current tracking-based assessment leads to several smooth hyperbolic curves with their unique geometric properties. Consequently, the alteration trend of these curves facilitates the Lyapunov coefficients to be adjusted commensurate with the dynamic operation of the converter while converging to zero steady-state errors. Using a TMS320F28335 digital signal processor (DSP), disparate experimental results are conducted on the SIDO-TLC to verify the accurate and robust performance of the proposed control strategy.**

**Keywords— Single-input dual-output three-level dc-dc converter (SIDO-TLC), direct Lyapunov strategy (DLS), output voltage variation, buck and boost outputs, Lyapunov coefficients.**

## I. INTRODUCTION

DC microgrids have earned a great deal of research interest due to the advancement in power electronics technology and penetration of renewable energy sources [1]– [4]. An important advantage of dc microgrids is the omission of the issues related to reactive power regulation and frequency synchronization, leading to a less complex control system [5], [6]. Multi-port dc-dc converters (MPC) are attractive solutions in dc micro-grids, as they can interact with different renewable energy sources and provide multiple dc outputs. Accordingly, MPCs can reduce the use of power electronic devices, enhancing energy and economic efficiency [7]– [10]. As yet, a large number of MPCs have been introduced, which are mainly practical for low voltage applications [11]– [19]. Nevertheless, for high voltage applications, the major challenge to MPCs is the voltage stress on switches. Therefore, high-rated switches are utilized to withstand the voltage stress, resulting in higher costs and conduction losses [20]. Moreover, to reduce losses, the switching frequency is practically limited to around 1 kHz, which causes the increased size of passive components [21], [22]. To overcome the abovementioned drawbacks, SIDO-TLC was introduced first by Ganjavi *et al.* [23]. As shown in Fig. 1, SIDO-TLC is an integration of the conventional three-level converter [24] with a multi-port converter [13]. Accordingly, SIDO-TLC requires a single dc source ($v_{in}$) to provide independent boost ($v_{o1}$) and buck ($v_{o2}$) output voltages. Indeed, through the three-level topology and control modulation, SIDO-TLC can decrease the voltage stress on switches and diodes to half of the output voltage and reduce the size of passive components [23], [25]. However, SIDO-TLC topology requires a complex controller to regulate two output voltages, balance the voltages across the output capacitors, and execute a three-level control modulation simultaneously. In [23], two proportional-integral (PI) compensators have been applied to SIDOTLC, which have critical issues such as the very slow dynamic and large overshoots/undershoots. Due to the unsatisfactory performance of PI compensators in achieving the desired control objectives, a feedback feed-forward (FB-FF) controller has been implemented on SIDO-TLC [26]. The experimental results in [26] prove that although the FB-FF controller significantly improved the dynamic performance at a limited operating range, it does not ensure fast dynamics and stability at a wide range of operations. Whereas, with the wide application of power electronic devices, including multiport dc-dc converters in future distribution systems, stability will be the principal objective in the power network control to maintain the operating equilibrium after major disturbances [27], [28].

The Lyapunov controller [29], [30] is a good nominee, which guarantees strict stability at a wide operating range and simplicity in implementation. In [29], the authors utilized a control strategy based on Lyapunov functions to ensure the stability of a cascade dc-dc converter. [30] presents a method to compute the switching control signals of the Cuk dc-dc converter using the Lyapunov theory. As far as our knowledge goes, very limited literature has applied the Lyapunov controller on multi-port dc-dc converters. For instance, Olm *et al.* [31] presented a control strategy to regulate the output voltages of a magnetically coupled multiport dc-dc converter using the Lyapunov stability theory. The theories presented in [31] are not implemented in the experiment. A challenge to the Lyapunov controller is achieving the fastest convergence rate for the Lyapunov function and robustness to the controller's coefficient variations [32]. Therefore, an effective method to select the coefficients of the Lyapunov function is desirable to obtain fast dynamics and stability in a wide range of operations.

In this paper, a direct Lyapunov strategy (DLS) is proposed to provide robust control loops for the SIDO-TLC exposed to the changes in the output loads and reference currents. The small-signal dynamic model of the SIDO-TLC aims to construct the DLS-based energy function for incorporating the proposed transient segments of the converter duty cycles into the well-adjusted Lyapunov coefficients. The contributions of this paper are described as follows,

- A new dynamic model with all passive energy-storage elements is achieved for the SIDO-TLC. In this regard, by splitting the total boost output voltage into two voltages across the capacitors $C_{11}$ and $C_{12}$, a comprehensive Lyapunov function is assigned for the dc-dc converter leading to the more detailed transient segments for the proposed control loops.
- For the first time, the Lyapunov strategy is applied to the SIDO-TLC. Compared to other strategies designed for the converter, the proposed control strategy can provide global stable performance for the SIDO-TLC in the presence of different load variation scenarios.
- The accuracy and robustness in the tracking ability of the inductor currents and output voltages for the stable operation of the SIDO-TLC are improved using the variation trend analysis of PI controller coefficients through mathematical calculations and 3-dimension (3D) curves.
- Hyperbolic curve-based evaluations are presented for realizing the allowable variations of Lyapunov coefficients focused on converging to zero inductor current errors.

This paper is organized as follows. The introduction is given in Section I. Section II explains the structure, large-signal model, and small-signal model of the SIDO-TLC. Subsequently, Section III is devoted to the design process of the DLS, along with analyzing the coefficients of the current reference controller. Consequently, the Lyapunov coefficient assessment is executed in section IV. Moreover, a lab prototype of the SIDO-TLC is built, and the proposed control technique is verified through the experimental results in section V. Finally, the conclusion of this study is provided in section VI.

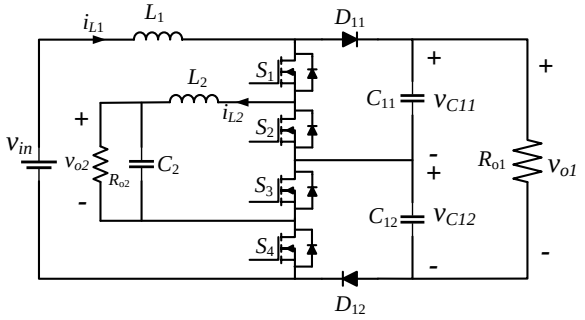


Fig. 1. The SIDO-TLC under study.

## II. Description of the SIDO-TLC Structure and Dynamic Model

Fig.1 shows the detailed structure of the SIDO-TLC, which will be discussed and analyzed in this paper. The converter consists of two boost and buck outputs with the voltages $v_{o1}$ and $v_{o2}$, respectively. These boost and buck segments possess the load resistance and inductance parameters, including $\{R_{o1}, L_1\}$ and $\{R_{o2}, L_2\}$, respectively. The converter comprises four power MOSFET switches and two power diodes named $\{S_1, S_2, S_3, S_4\}$ and $\{D_{11}, D_{12}\}$, respectively. Moreover, all the possible switching states of the converter are shown in Table 1. Furthermore, there are three modes of operation for the SIDO-TLC represented by case *A*, case *B*, and case *C*, which have been completely explained in [23]. In addition, more details regarding the switching sequences of the SIDO-TLC can be found in [26]. In this paper, only case *A* is taken into account. As a consequence, there are two duty cycles of $d_1$ and $d_2$ in case A, which are employed in PWM control according to Fig. 2. Accordingly, the duty cycles are exerted on the switches $\{S_1, S_3\}$ and $\{S_2, S_4\}$ with no phase shifting and 180-degree phase shifting, respectively. It is worth mentioning from [23] that the boost and buck voltage gains of the converter are equalized to (1) and (2), respectively.

$$g_{o1} = \frac{v_{o1}}{v_{in}} = \frac{1}{2 - d_1 - d_2} \tag{1}$$

$$g_{o2} = \frac{v_{o2}}{v_{in}} = \frac{1 - d_2}{2 - d_1 - d_2} \tag{2}$$

Table 1: The switching states of the SIDO-TLC.

| Switching States | $S_1$ | $S_2$ | $S_3$ | $S_4$ |
|---|---|---|---|---|
| 1 2 3 4 | 0000 | 0011 | 0101 | 0000 |
| 5 6 | 00 | 01 | 11 | 11 |
| 7 8 | 1 1 | 1 1 | 0 1 | 0 0 |
| 9 10 | 0 0 | 0 1 | 0 0 | 1 1 |
| 11 12 | 1 1 | 0 0 | 0 1 | 0 0 |
| 13 | 1 | 0 | 1 | 1 |
| 14 | 1 | 1 | 0 | 1 |
| 15 | 1 | 0 | 0 | 1 |

Based on (1) and (2), it can be concluded that the two duty cycles are dependent on the gains as $d_1 = 1 - g_{o1}^{-1} + g_{o2} \times g_{o1}^{-1}$ and $d_2 = 1 - g_{o2} \times g_{o1}^{-1}$. Also, the dynamic equations of (3)-(7) describe the large signal model of the SIDO-TLC.

$$L_1 \frac{di_{L1}}{dt} = d_1 V_{o1} + d_2 V_{o1} + 2\Delta d \Delta V_c + V_{in} - 2V_{o1} \tag{3}$$

$$L_2 \frac{di_{L2}}{dt} = -d_2 V_{o1} - \Delta d \Delta V_c + V_{o1} - V_{o2} \tag{4}$$

$$C_1 \frac{dV_{o1}}{dt} = -2d_1 i_{L1} + 2(i_{L2} - i_{L1})d_2 + 2(2i_{L1} - i_{L2}) - \frac{2V_{o1}}{R_{o1}} \tag{5}$$

$$C_2 \frac{dV_{C2}}{dt} = i_{L2} - \frac{V_{o2}}{R_{o2}} \tag{6}$$

$$C_1 \frac{d\Delta V_C}{dt} = 2(-2i_{L1} + i_{L2})\Delta d \tag{7}$$

After extending (3)-(7), the initial small-signal dynamic model of the SIDO-TLC in Fig. 1 is acquired as follows [23].

$$\frac{d\hat{i}_{L1}}{dt} = \frac{(D_1 + D_2 - 2)}{L_1}\hat{v}_{o1} + \frac{2\Delta D}{L_1}\Delta\hat{v}_c + \frac{v_{o1}^*}{L_1}\hat{d}_1 + \frac{v_{o1}^*}{L_1}\hat{d}_2 + \frac{2\Delta V_c}{L_1}\Delta\hat{d} + \frac{\hat{v}_{in}}{L_1} \tag{8}$$

$$\frac{d\hat{i}_{L2}}{dt} = \frac{(1 - D_2)}{L_2}\hat{v}_{o1} - \frac{1}{L_2}\hat{v}_{o2} - \frac{\Delta D}{L_2}\Delta\hat{v}_c - \frac{v_{o1}^*}{L_2}\hat{d}_2 - \frac{\Delta V_c}{L_2}\Delta\hat{d} \tag{9}$$

$$\frac{d\hat{v}_{o1}}{dt}=\frac{-2\left(D_1+D_2-2\right)}{C_1}\hat{i}_{L1}-\frac{2\left(1-D_2\right)}{C_1}\hat{i}_{L2}-\frac{2}{R_{o1}C_1}\hat{v}_{o1}$$
$$-\frac{2i^*_{L1}}{C_1}\hat{d}_1+\frac{2\left(i^*_{L2}-i^*_{L1}\right)}{C_1}\hat{d}_2 \quad (10)$$

$$\frac{d\hat{v}_{o2}}{dt}=\frac{1}{C_2}\hat{i}_{L2}-\frac{1}{R_{o2}C_2}\hat{v}_{o2} \quad (11)$$

$$\frac{d\Delta\hat{v}_c}{dt}=\left(-\frac{4\Delta D}{C_1}\right)\hat{i}_{L1}+\left(\frac{2\Delta D}{C_1}\right)\hat{i}_{L2}+\left(\frac{2\left(i^*_{L2}-2i^*_{L1}\right)}{C_1}\right)\Delta\hat{d} \quad (12)$$

Where $\hat{x}=x-x^*$ and also $x$ is member of $\{i_{L1}, i_{L2}, v_{o1}, v_{o2}, v_{in}, \Delta v_c\}$. In addition, $\Delta\hat{v}_c=v_{C11}-v_{C12}$ is the balancing voltage of the boost output. In the dynamic equations (8)-(12), the duty cycles are defined according to $\hat{d}_1=d_1-D_1$, to $\hat{d}_2=d_2-D_2$ and $\Delta\hat{d}=\Delta d-\Delta D$. The parameter $\Delta\hat{d}$ is regarded as the balancing duty cycle to converge the difference between $v_{C11}$ and $v_{C12}$ to zero.

## III. Proposed Control Technique

Direct Lyapunov strategy (DLS) is employed in this paper to design an effective control strategy with an acceptable stability margin for the SIDO-TLC shown in Fig. 1. Noticing the SIDO-TLC, the proposed control strategy aims to use the dynamics of all passive energy-storage elements including the capacitor voltages and the inductor currents. To this end, the errors for designing DLS are firstly redefined just as $z_{L1}=i_{L1}-i^*_{L1}$, $z_{L2}=i_{L2}-i^*_{L2}$, $z_{C2}=v_{o2}-v^*_{o2}$, $z_{C11}=v_{C11}-v^*_{C11}$, and $z_{C12}=v_{C12}-v^*_{C12}$. By applying the redefined errors to the initial dynamic equations in (8)-(12), the new dynamic model based on the state variables of all passive energy-storage elements is obtained with the matrix representation in (13),

$$\frac{d}{dt}\begin{bmatrix}L_1z_{L1}\\L_2z_{L2}\\C_1z_{C11}\\C_1z_{C12}\\C_2z_{C2}\end{bmatrix}=\begin{bmatrix}0 & 0 & \begin{pmatrix}D_1+D_2\\-2+2\Delta D\end{pmatrix} & \begin{pmatrix}D_1+D_2\\-2-2\Delta D\end{pmatrix} & 0\\ 0 & 0 & \begin{pmatrix}1-D_2\\-\Delta D\end{pmatrix} & \begin{pmatrix}1-D_2\\+\Delta D\end{pmatrix} & -1\\ \begin{pmatrix}2-2\Delta D\\-D_1-D_2\end{pmatrix} & \begin{pmatrix}\Delta D-1\\+D_2\end{pmatrix} & \begin{pmatrix}-1\\R_{o1}\end{pmatrix} & \begin{pmatrix}-1\\R_{o1}\end{pmatrix} & 0\\ \begin{pmatrix}2+2\Delta D\\-D_1-D_2\end{pmatrix} & \begin{pmatrix}-1+D_2\\-\Delta D\end{pmatrix} & \begin{pmatrix}-1\\R_{o1}\end{pmatrix} & \begin{pmatrix}-1\\R_{o1}\end{pmatrix} & 0\\ 0 & 1 & 0 & 0 & \begin{pmatrix}-1\\R_{o2}\end{pmatrix}\end{bmatrix}\begin{bmatrix}z_{L1}\\z_{L2}\\z_{C11}\\z_{C12}\\z_{C2}\end{bmatrix}$$
$$+\begin{bmatrix}v_{o1}^* & v_{o1}^* & 2\Delta V_C\\ 0 & -v_{o1}^* & -\Delta V_C\\ -i_{L1}^* & (i_{L2}^*-i_{L1}^*) & (i_{L2}^*-2i_{L1}^*)\\ -i_{L1}^* & (i_{L2}^*-i_{L1}^*) & -(i_{L2}^*-2i_{L1}^*)\\ 0 & 0 & 0\end{bmatrix}\begin{bmatrix}\hat{d}_1\\\hat{d}_2\\\Delta\hat{d}\end{bmatrix}+\begin{bmatrix}\hat{v}_{in}\\0\\0\\0\\0\end{bmatrix} \quad (13)$$

If the Lyapunov function $V(z)$ is taken into account, the stability of the system can be investigated around its equilibrium points by satisfying the conditions detailed in (14),

$$\begin{cases}V(z)=0 \quad for\ z=0\\ V(z)>0 \quad for\ z\neq 0\\ \lim\limits_{x\to\infty}V(z)=\infty\\ \dot{V}(z)<0 \quad for\ z\neq 0\end{cases} \quad (14)$$

In the considered SIDO-TLC, the equilibrium points of interest are the members of $\{i^*_{L1}, i^*_{L2}, v^*_{o2}, v^*_{C11}, v^*_{C12}\}$. Accordingly, the Lyapunov function must be assessed to provide the asymptotically stable performance of the converter under various operating conditions. In this paper, the Lyapunov function is defined as the sum of the stored energy in the inductors and capacitors of the SIDO-TL converter based on (15),

$$V(z)=\frac{1}{2}L_1{z_{L1}}^2+\frac{1}{2}L_2{z_{L2}}^2+\frac{1}{2}C_1{z_{C11}}^2+\frac{1}{2}C_1{z_{C12}}^2+\frac{1}{2}C_2{z_{C2}}^2 \quad (15)$$

In the first step, it can be realized that the Lyapunov function (15) assures the first three parts of the condition (14). Subsequently, the time-based derivative of (15), along with using the dynamic model of (13), leads to the following summarized terms for the Lyapunov function derivation,

$$\frac{dV(z)}{dt}=\hat{v}_{in}z_{L1}-(i_{L1}{}^*(z_{C11}+z_{C12})-v_{o1}{}^*z_{L1})\hat{d}_1+$$
$$(v_{o1}{}^*(z_{L1}-z_{L2})+(i_{L2}{}^*-i_{L1}{}^*)(z_{C11}-z_{C12}))\hat{d}_2$$
$$+(\Delta V_C(2z_{L1}-z_{L2})+(i_{L2}{}^*-2i_{L1}{}^*)(z_{C11}-z_{C12}))\Delta\hat{d} \quad (16)$$
$$-\frac{1}{R_{o2}}{z_{C2}}^2-\frac{1}{R_{o1}}(z_{C12}+z_{C11})^2$$

In order that $dV(z)/dt$ definitely gets negative for $z\neq 0$, the duty cycle errors of the SIDO-TLC must be equalized to (17) after extending (16),

$$\begin{cases}\begin{pmatrix}\hat{d}_1=\alpha_1(-z_{L1}v^*_{o1}+\\ i^*_{L1}(z_{C11}+z_{C12}))\end{pmatrix}, \alpha_1>\dfrac{\hat{v}_{in}z_{L1}}{\begin{pmatrix}i_{L1}{}^*(z_{C11}+z_{C12})\\ -v_{o1}{}^*z_{L1}\end{pmatrix}^2}\ \&\ \alpha_1>0\\ \begin{pmatrix}\hat{d}_2=-\alpha_2(v^*_{o1}(z_{L1}-z_{L2})\\ +(i^*_{L2}-i^*_{L1})(z_{C11}-z_{C12}))\end{pmatrix} \quad \alpha_2>0\\ \begin{pmatrix}\Delta\hat{d}=-\alpha_3(\Delta V_C(2z_{L1}-z_{L2})\\ +(i^*_{L2}-2i^*_{L1})(z_{C11}-z_{C12})),\end{pmatrix} \quad \alpha_3>0\end{cases} \quad (17)$$

Where $\alpha_1$, $\alpha_2$, and $\alpha_3$ are the Lyapunov coefficients that should be adjusted to align with the operating condition requirements. If the dynamic parts of the duty cycles are formulated according to (17), the asymptotical stability margin is guaranteed for the proposed Lyapunov-based SIDO-TLC. Accordingly, strict stability is obtained even when errors for SIDO-TLC state variables exist. The ultimate duty cycles are established through $d_1=\hat{d}_1+D_1$, $d_2=\hat{d}_2+D_2$ and $\Delta d=\Delta\hat{d}+\Delta D$. Notably, $S_1$–$S_4$ is determined through $d_{s1}=d_1+\Delta d$, $d_{s2}=d_2+\Delta d$, $d_{s3}=d_1-\Delta d$, and $d_{s4}=d_1-\Delta d$, respectively shown in Fig. 1. The block diagram of the proposed method is depicted in Fig. 2. As can be seen, the reference values of the $L_1$ and $L_2$ currents are driven by passing, respectively, the boost and buck voltage errors from the PI controllers. The PI controller coefficients are analyzed in the following sub-section.

### A. Analysis of Reference Current Controller Coefficients

The reference values of the SIDO-TLC inductor currents are determined by passing the buck and boost voltage errors from two PI controllers with the proportional and integral coefficients $\{k_{p1}, k_{i1}\}$ and $\{k_{p2}, k_{i2}\}$, respectively. Therefore, it is crucial to understand how these coefficients should be altered to achieve minimal errors.

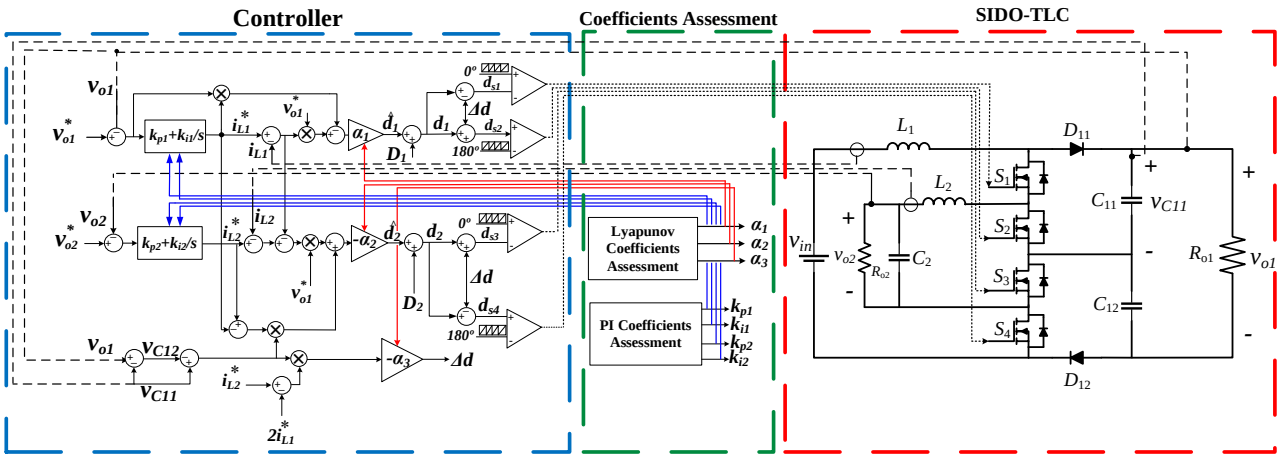


Fig. 2. Proposed Lyapunov direct strategy bock diagram for SIDO-TLC

If the duty cycle errors in (17) tend to zero (i.,e. $\hat{d}_1 = \hat{d}_2 = \Delta\hat{d} \simeq 0$), the SIDO-TLC will attain a stable performance made up of desirable transient repercussions. Exerting this assumption to the two first terms of (17) (considering the condition $\alpha_{1(2)} \neq 0$), the inductor current errors are achieved according to (18).

$$\begin{cases} z_{L1} = i_{L1} - i^*_{L1} = \dfrac{i^*_{L1}(z_{C11} + z_{C12})}{v^*_{o1}} \\ z_{L2} = i_{L2} - i^*_{L2} = z_{L1} + \dfrac{(i^*_{L2} - i^*_{L1})(z_{C11} - z_{C12})}{v^*_{o1}} \end{cases} \tag{18}$$

The following relations are obtained by substituting the inductor current references from Fig. 2 into (18).

$$\begin{cases} \left(v^*_{o1} + z_{C1}\right) z_{C1} k_{i1} + \left(v^*_{o1} + 2z_{C1}\right) \dot{z}_{C1} k_{p1} + v^*_{o1} \dot{i}_{L1} = 0 \\ \left((z_{C12} - z_{C11})\dot{z}_{C2} - v^*_{o1}\dot{z}_{C2} + (\dot{z}_{C12} - \dot{z}_{C11}) z_{C2}\right) k_{p2} \\ + \left(-v^*_{o1} + z_{C12} - z_{C11}\right) z_{C2} k_{i2} \\ +2\left(-z_{C12}\dot{z}_{C1} - \dot{z}_{C12} z_{C1}\right) k_{p1} + 2\left(-z_{C12} z_{C1}\right) k_{i1} - v^*_{o1} \dot{i}_{L2} = 0 \end{cases} \tag{19}$$

Neglecting the ripples of the output voltage errors ( $\dot{z}_{C1} = \dot{z}_{C2} = \dot{z}_{C11} = \dot{z}_{C12} = 0$ ), the relations in (19) will result in the following integral coefficients.

$$\begin{cases} k_{i1} = \dfrac{-v^*_{o1} \dot{i}_{L1}}{\left(v^*_{o1} + z_{C1}\right) z_{C1}} \\ k_{i2} = \dfrac{-2v^*_{o1} z_{C12} \dot{i}_{L1} + v^*_{o1}\left(v^*_{o1} + z_{C1}\right) \dot{i}_{L2}}{\left(-v^*_{o1} + z_{C12} - z_{C11}\right)\left(v^*_{o1} + z_{C1}\right) z_{C2}} \end{cases} \tag{20}$$

The integral coefficients in (20) can help the ultimate control technique provide more suitable transient responses. However, a complete assessment can be made for both integral and proportional coefficients simultaneously without assuming the zero ripple for the voltage errors. To this end, two equations of (19) are firstly rearranged in the manner of (21) and (22), respectively.

$$k_{p1} = f\left(k_{i1}, z_{C1}, \dot{z}_{C1}\right) \tag{21}$$

$$k_{p2} = f\left(k_{i2}, z_{C2}, \dot{z}_{C2}\right) + H\left(k_{i1}, z_{C1}, z_{C11}, z_{C12}, \dot{z}_{C11}, \dot{z}_{C12}\right) \tag{22}$$

Using equations (21) and (22), the variation trend of the integral and proportional coefficients is plotted through the 3D curves based on their related errors in different operating points, as depicted in Fig. 3. Accordingly, different supra-index refers to the different values of $\frac{dz_{C1}}{dt}$ and $\frac{dz_{C2}}{dt}$ .

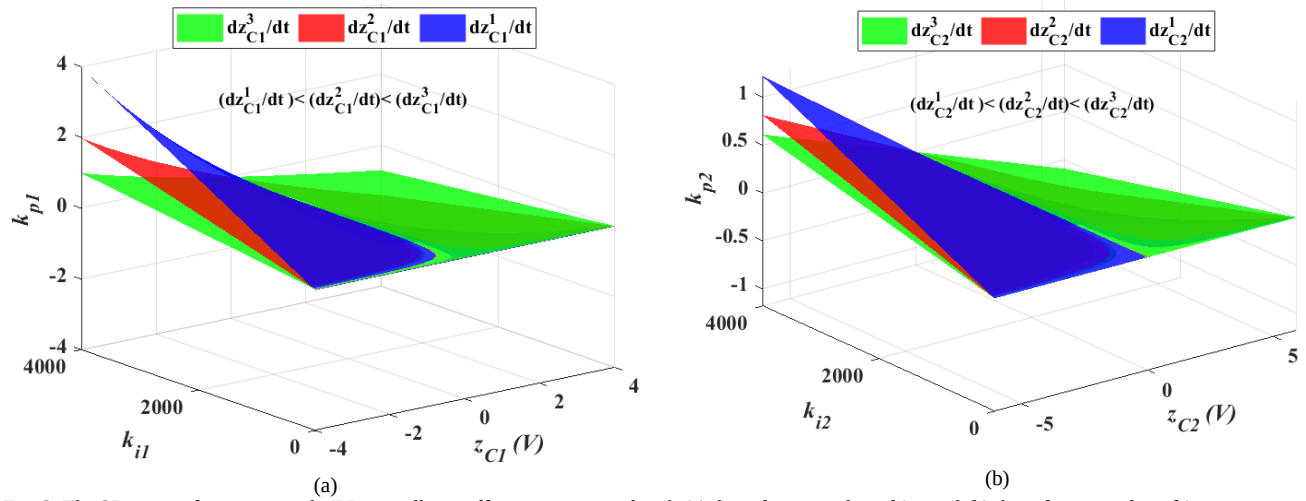


(a) (b)

Fig. 3. The 3D curves for assessing the PI controller coefficients associated with (a) the reference value of $i_{L1}$, and (b) the reference value of $i_{L2}$.

To analyze the results depicted in Fig. 3, the integral coefficients should be obtained from (20). According to this figure, the proportional coefficients are increased with a decrease in the derivative of the errors. Also, bigger proportional coefficients are needed for the PI controllers when the magnitude of the minus voltage errors for $z_{C1}$ and $z_{C2}$ is increased, as depicted in Fig. 3. However, the relations in (20) aim to assign the initial acceptable values for the integral coefficients, but, the additional assessments through Fig. 3 can help the proposed control strategy reach more effective dynamic proportional coefficients by taking the integral coefficients and the voltage errors into account. To summarize this section, in a full load condition, for instance, for the PI controller's coefficients, first, the instantaneous values of $k_{i1}$ and $k_{i2}$ are obtained using (20). Subsequently, the instantaneous values of $k_{p1}$ and $k_{p2}$ are selected based on the values of $k_{i1}$ and $k_{i2}$ in Fig.3.

## IV. Lyapunov Coefficients Assessment

The Lyapunov coefficients must be appropriately adjusted to enable the proposed control strategy to perform effectively in various operating conditions. Hence, the impact of the Lyapunov coefficients including $\alpha_1$, $\alpha_2$, and $\alpha_3$ on the errors $z_{L1}$ and $z_{L2}$ is comprehensively assessed in this section. In this regard, the dynamic portions of the duty cycles in (17) are substituted into the current error dynamics of SIDO-TLC in (13), resulting in (23) and (24).

$$\begin{aligned} L_1\frac{dz_{L1}}{dt} &= (D_1+D_2-2+2\Delta D)(z_{C1}+z_{C2})+\alpha_1 v^*_{o1} i^*_{L1} z_{o1} \\ &-(\alpha_1+\alpha_2)v^*_{o1}{}^2 z_{L1}+\alpha_2 v^*_{o1}{}^2 z_{L2} \\ &-\alpha_2 v^*_{o1}(i^*_{L2}-i^*_{L1})(z_{C1}-z_{C2})+\hat{v}_{in} \end{aligned} \tag{23}$$

$$\begin{aligned} L_2\frac{dz_{L2}}{dt} &= (1-D_2)z_{o1}-z_{o2}z_{L2}+\alpha_2 v^*_{o1}{}^2 z_{L1}-\alpha_2 v^*_{o1}{}^2 z_{L2} \\ &+\alpha_2 v^*_{o1} i^*_{L2}(z_{C1}-z_{C2})-\alpha_2 v^*_{o1} i^*_{L1}(z_{C1}-z_{C2}) \end{aligned} \tag{24}$$

Subsequently, (23) and (24) are multiplied by $z_{L1}$ and $z_{L2}$, respectively. Then, after simplifications, a hyperbolic curve is formulated in (25), as depicted in Fig. 4. In this figure, parameters *F* and *V* are denoted as *foci* and *vertices*, respectively.

$$\frac{(z_{L2}-z_{L2,0})^2}{a^2}-\frac{(z_{L1}-z_{L1,0})^2}{b^2}=K \tag{25}$$

Where the parameters in (25) are given as follows,

$$\begin{aligned} &a=\sqrt{\left|\frac{A_2B_1{}^2-A_1{}^2B_2}{4A_2B^2{}_2}\right|}, b=\sqrt{\left|\frac{A_2B_1{}^2-A_1{}^2B_2}{4A^2{}_2B_2}\right|} \\ &c=\sqrt{a^2+b^2}, z_{L1,0}=-(\frac{A_1}{2A_2}), z_{L2,0}=(\frac{B_1}{2B_2}), K=\pm 1 \\ &A_1=-[(D_1+D_2-2+(\alpha_1+\alpha_2)v^*_{o1}i_{L1}{}^*-\alpha_2 v^*_{o1}i_{L2}{}^*)z_{C1}+\hat{v}_{in} \\ &+(D_1+D_2-2+(\alpha_1-\alpha_2)v^*_{o1}i_{L1}{}^*+\alpha_2 v^*_{o1}i_{L2}{}^*))z_{C2}-L_1\frac{dz_{L1}}{dt}] \\ &B_1=-[z_{o2}-(1-D_2+\alpha_2 v_{o1}{}^*(i_{L2}{}^*-i_{L1}{}^*))z_{C1} \\ &-(1-D_2-\alpha_2 v_{o1}{}^*(i_{L2}{}^*-i_{L1}{}^*))z_{C2}+L_2\frac{dz_{L2}}{dt}] \\ &A_2=(\alpha_1+\alpha_2)v_{o1}{}^{*2}, B_2=\alpha_2 v_{o1}{}^{*2} \end{aligned} \tag{26}$$

It should be noted that the cases *K*=1 and *K*=-1 will be made when the inequalities $\frac{A_2B_1{}^2-A_1{}^2B_2}{4A_2B^2{}_2}>0$ and $\frac{A_2B_1{}^2-A_1{}^2B_2}{4A_2B^2{}_2}<0$ are satisfied, respectively. Furthermore, when *K=1*, the transverse axis of the hyperbolic curve lies on $z_{L2}$-axis with center coordinates of ($z_{L2,0}$, $z_{L1,0}$) as depicted in Fig. 4. On the contrary, for *K*=-1, the transverse axis of the hyperbolic curve is upon $z_{L1}$-axis, and its center is on ($z_{L1,0}$, $z_{L2,0}$) point, accordingly. Considering Fig. 4, both $z_{L1}$ and $z_{L2}$ errors move on the branches of the hyperbolic curve.

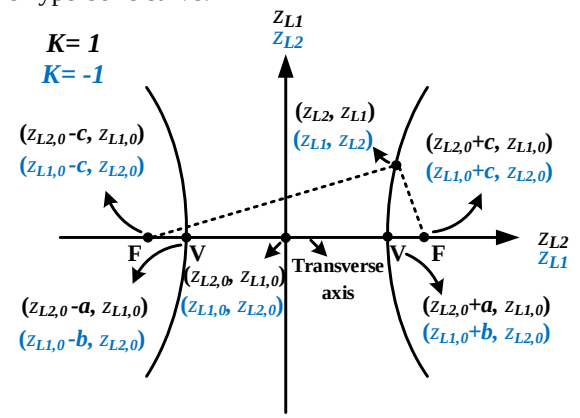


Fig. 4. The hyperbolic curve based on $z_{L1}$ and $z_{L2}$.

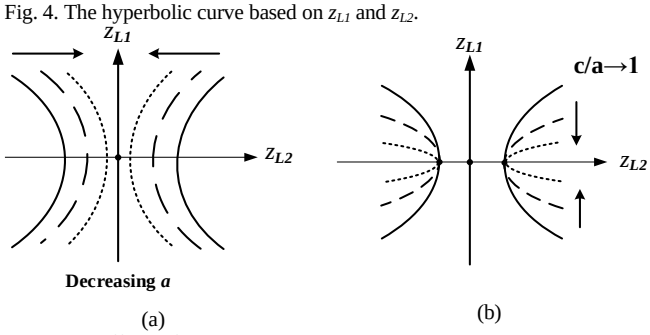


Fig. 5. The effects of the hyperbolic curve parameters on the errors $z_{L1}$ and $z_{L2}$ (a) when *a* is decreased, and (b) when $(c/a)\rightarrow 1$.

As shown in Fig. 5(a), when the branches of the hyperbolic curve are forced to move toward the $z_{L1}$-axis (in the case of *K*=1), the error $z_{L2}$ decreases. This trend is feasible by gradually reducing the parameter *a* towards zero ($a\rightarrow 0$). In the following, it can be realized from Fig. 5(b) that when the hyperbolic branches move toward $z_{L2}$-axis, the error $z_{L1}$ is reduced accordingly. This state is guaranteed by satisfying the conditions $(c/a)\rightarrow 1$ or $a >> b$. Considering the explanations above and the relation (26), it can be concluded that:

$$if\ a>>b \Rightarrow \frac{1}{A_2}<<\frac{1}{B_2}\rightarrow \alpha_1>>\alpha_2 \tag{27}$$

Similarly, using the same analysis for *K*=-1, the errors $z_{L1}$ and $z_{L2}$ are diminished with respectively satisfying the conditions of $\{(c/b)\rightarrow 1$ or $b >> a\}$ and $\{b\rightarrow 0\}$, yielding (28).

$$if\ b>>a \Rightarrow \frac{1}{A_2}>>\frac{1}{B_2}\rightarrow \alpha_1<<0 \tag{28}$$

To attain the stability criteria for the Lyapunov function in (14) (as ascertained in (17)), the inequalities in (28) cannot be realized since the Lyapunov coefficient $\alpha_1$ must be strictly positive. For this purpose, the condition *K*=-1 must be prevented, leading to the inequality of (29).

$$\frac{A_2B_1^2 - A_1^2B_2}{4A_2B_2^2} > 0 \Rightarrow \begin{cases} \begin{cases} A_2 > A_1^2B_2 / B_1^2 \\ A_2 > 0 \end{cases} \\ or \\ \begin{cases} A_2 < A_1^2B_2 / B_1^2 \\ A_2 < 0 \end{cases} \end{cases} \quad (29)$$

As realized from (26), only the first set of inequalities in (29) is acceptable since $A_2$ and $B_2$ are always positive. Assuming that the system has stable performance, the errors (due to the proposed technique) fluctuate around the zero value ( $|z_{L1}|, |z_{L2}| << 1$), leading to the inequalities of $A_1 << A_2$ and $B_1 << B_2$ in (26), meaning that $z_{L1,0} = z_{L2,0} \simeq 0$. Accordingly, Fig.6 (a) and (b) show how the Lyapunov coefficients of $\alpha_1$ and $\alpha_2$ can impact the parameters of *a* and *b*, respectively. Consequently, an increment in either $\alpha_1$ or $\alpha_2$ will decrease both parameters of *a* and *b*. In addition, as it can be understood from (26), the errors of $z_{L1}$ and $z_{L2}$ cannot be affected by the coefficient $\alpha_3$ relying on the analysis obtained from the hyperbolic curve shown in Fig. 4.

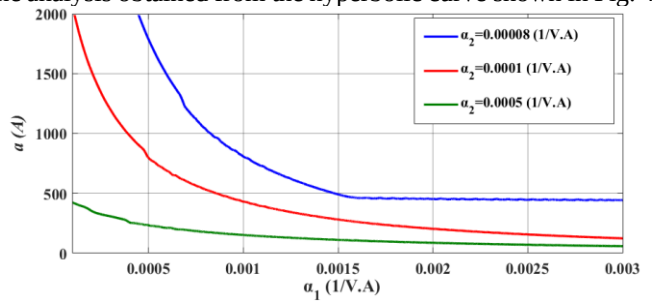


(a)

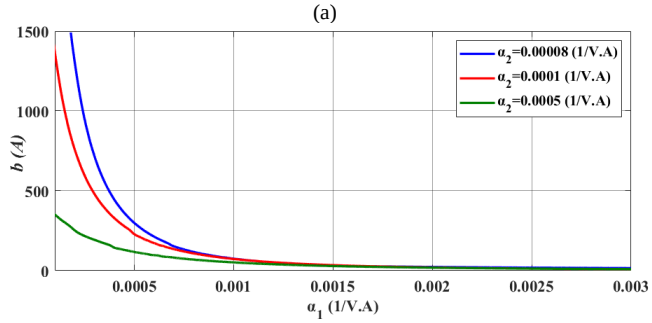


(b)

Fig. 6. The effect of $\alpha_1$ and $\alpha_2$ on the hyperbolic curve parameters (a) parameter *a* and (b) the parameter *b*.

## V. EXPERIMENTAL RESULTS

This section focuses on the experimental verification of the proposed control technique implemented in the lab prototype of the SIDO-TLC during both steady and dynamic states. As shown in Fig. 7, a digital signal processor (DSP) TMS320F28335 from Texas Instruments is utilized to make the required pulses based on the phase-shifted PWM strategy. Moreover, the generated pulses are amplified through buffer ICs (74HC244P), and the isolation between the power and control systems is developed by a Driver/Optocoupler IC (HCPL3120). The following is organized to discuss the different operating scenarios exerted on the experimental setup illustrated in Fig. 7. Accordingly, Table II determines the detailed parameters of the experimental prototype.

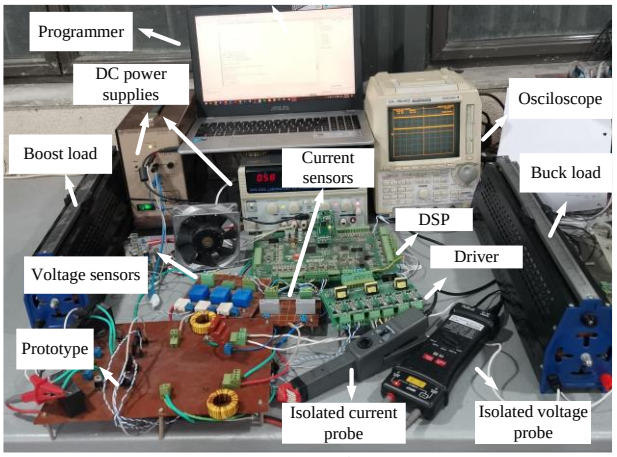


Fig. 7. The experimental test setup used for the proposed controller-based prototype SIDO-TLC.

Table II: The detailed parameters of the experimental Prototype.

| Parameters | Value |
|---|---|
| Input voltage | 12 V |
| Buck output voltage | 9 V |
| Boost output voltage | 24 V |
| Buck output capacitors | 100 (µF) |
| Boost output capacitors | 2×100 (µF) |
| MOSFET Model | IRLR3715ZPbF |
| Diode Model | MBR1635 |
| Inductor $L_1$ | 211 µH |
| Inductor $L_2$ | 363 µH |
| Sampling Time | 50 µs |
| Switching Frequency | 20 kHz |

In addition, the instantaneous coefficient values of the PI controller are selected based on (20). Besides, the Lyapunov coefficients boundaries condition resulting from (17), (27), and (29) are shown in Fig. 8 for a full load condition. In this test, the ripple coefficients of the output voltage, the inductors currents, and the input voltage are equalized to $\delta_{vout}$=0.05, $\delta_{iL1}$=0.20, $\delta_{iL2}$=0.20, and $\delta_{vin}$=0.01. Using (1) and (2), the duty ratios of $d_1$ and $d_2$ are obtained as 0.875 and 0.625, respectively. Subsequently, the current reference value of inductor $L_1$ ($i_{L1}^*$) is approximated to 1.84A based on the output loads. Furthermore, the errors including $z_{C1}$, $z_{L1}$, $\hat{v}_{in}$, $\Delta\hat{v}_c$ are estimated as 0.6V, ±0.195A, 0.06V, 0.6V, respectively. Also, the values of $L_1 d\hat{i}_{L1}/dt$ and $L_2 d\hat{i}_{L2}/dt$ are almost zero.

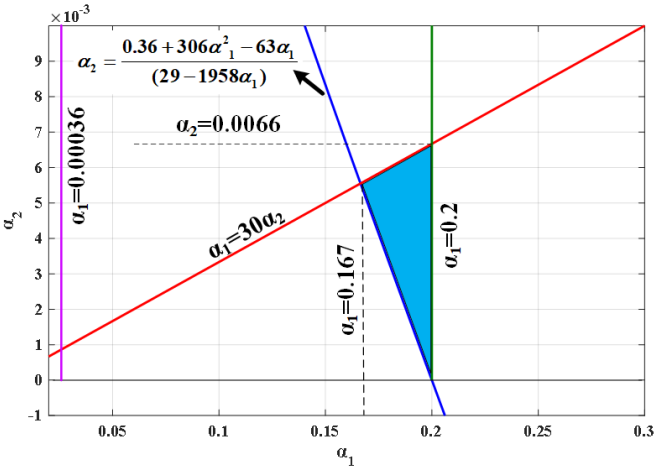


Fig. 8. Lyapunov coefficients $\alpha_1$ and $\alpha_2$ boundaries.

### A. Reference alteration of the output voltages

This section concentrates on the dynamic responses of the proposed control strategy implemented on the SIDO-TLC when the reference values of the boost and buck output voltages are altered. Before that, by considering the boost and buck output resistive loads respectively as $R_{o1}$=44Ω and $R_{o2}$=9Ω, the steady-state response is presented in Fig. 9, wherein both output voltages can accurately track their desirable values ($v_{o1}$=24V and $v_{o2}$=9V). In addition, the inductors currents ($i_{L1}$ and $i_{L2}$) achieve acceptable performance with stable waveforms, as depicted in Fig. 9. Furthermore, Fig. 10 illustrates the transient responses of the SIDO-TLC under the step variation of the reference value for the boost output voltage from 28 V to 24 V. Accordingly, it can be realized from this figure that the boost voltage can be decreased appropriately to 24 V with a good transient time and consequently a part of the boost output voltage of $C_{11}$ can be proportionally reduced as well. The point beyond this scenario is that the inductor current $i_{L1}$ can be smoothly adapted to reach the strict tracking capability through the proposed Lyapunov strategy. It is worth noting that the step change at the reference value of the boost output voltage cannot impact the stability and smooth response of the buck output voltage, as seen in Fig. 10.

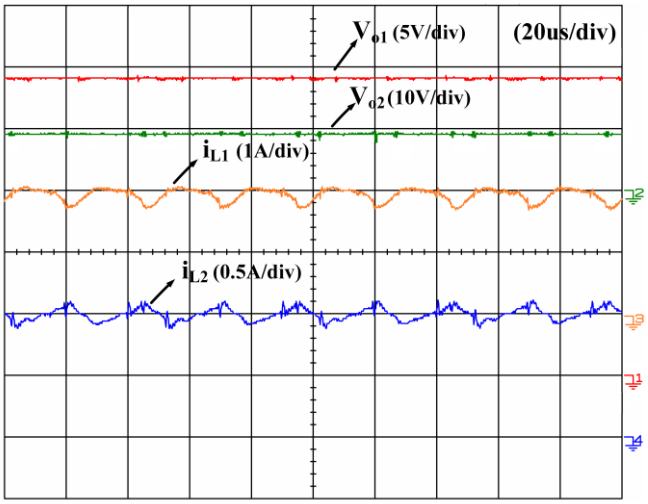


Fig. 9. Steady-state responses of the SIDO-TLC.

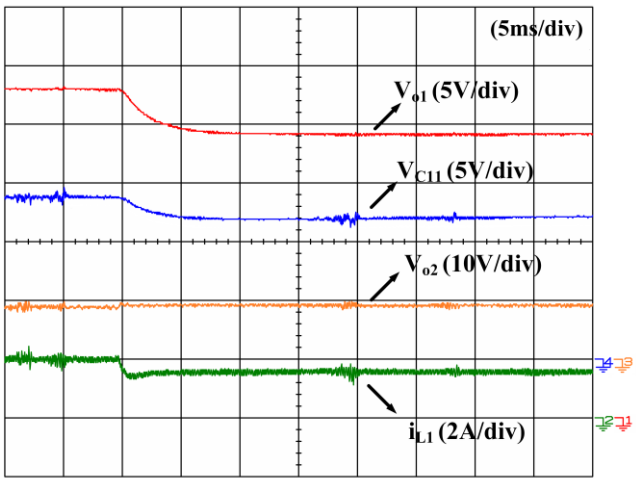


Fig. 10. The step change of the boost output voltage's reference from $v^*_{o2}$=28 V to $v^*_{o2}$=24 V.

In another scenario, the reference value of the buck output voltage is increased from 7 V to 9 V. In this condition, both experimental steady and dynamic responses of the SIDO-TLC under the proposed Lyapunov strategy are indicated in Fig. 11. According to this figure, the buck output voltage is increased to 9 V with an acceptable transient time. To provide further smooth variation, the reference step change of the buck output voltage can enable the inductor current $i_{L2}$ to be proportionally increased. In this scenario, the tracking ability of the proposed control strategy can be more verified when the experimental results of the boost output voltage ($v_{o1}$) and the first balancing voltage ($v_{C11}$) are assessed accordingly. As shown in Fig. 11, the voltages $v_{o1}$ and $v_{C11}$ are quite stable when the buck output voltage reference value is suddenly increased.

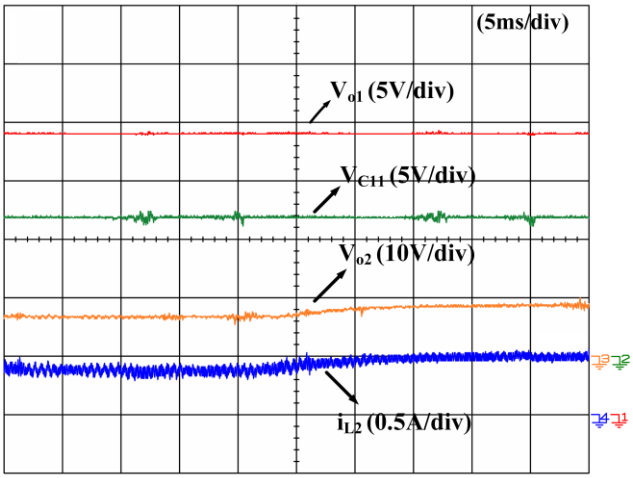


Fig. 11. The step change of the buck output voltage's reference from $v^*_{o2}$=7 V to $v^*_{o2}$=9 V.

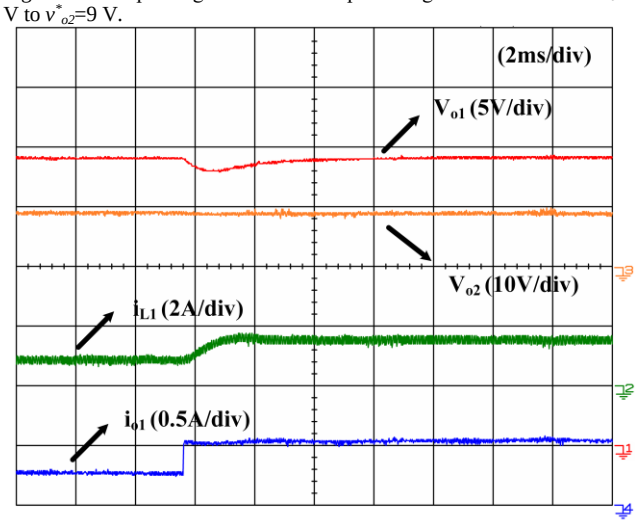


Fig. 12. Dynamic response of the proposed controller-based SIDO-TLC under the step change of the boost output load which changes from $R_{o1}$=64 Ω to $R_{o1}$=44 Ω.

### B. load alteration

In this sub-section, the proposed controller is evaluated in terms of a load variation occurring in both buck and boost outputs. Accordingly, Fig. 12 illustrates the transient responses of the proposed control-based SIDO-TLC when the boost output load ($R_{o1}$) changes from 64 Ω to 44 Ω, and the buck output load ($R_{o2}$) remains constant at 18 Ω. As can be noticed in this figure,

the boost output voltage ($V_{o1}$) perfectly tracks the reference value after an acceptably small undershoot at the load alteration. Moreover, the buck output voltage is completely regulated to be 9 V during the step change of load. Also, the inductor current $i_{L1}$ is appropriately stable and varies smoothly during the load step change with the help of the proposed Lyapunov-based control. Subsequently, Fig. 13 illustrates the dynamic performance of the proposed controller after a sudden change in the buck output load. In this test, $R_{o2}$ varies from 36 Ω to 18 Ω while $R_{o1}$ is considered as a constant value of 44 Ω. It should be noted that the proposed controller can appropriately regulate the buck and boost output voltages at their desired values with a slight undershoot at the exact moment of the load step change. In such conditions, the inductors currents of $i_{L1}$ and $i_{L2}$ demonstrate a smooth dynamic response.

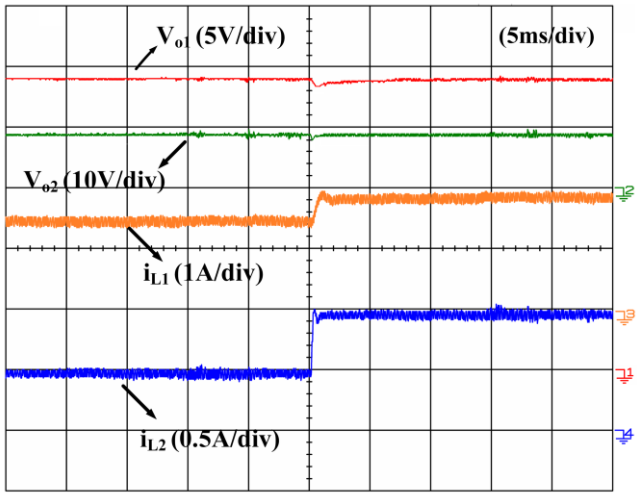


Fig. 13. Dynamic response of the proposed controller-based SIDO-TLC under the step change of the buck output load when changes from $R_{o2}$=36 Ω to $R_{o2}$=18.

## VI. Conclusion

This paper has presented a direct Lyapunov strategy (DLS) for the SIDO-TLC by utilizing the corresponding dynamic small-signal equations by taking the variations of the loads and voltage references into consideration. Several investigations have been carried out to increase the robustness and accuracy of the proposed control technique's performance against these variations. The proposed strategy has considered the principles originating from the dynamic model of the SIDO-TLC, the mathematical equations of the reference currents, and the proposed dynamic components of the duty cycles. To this end, the variation trend analysis of the PI controller coefficients within the related mathematical calculations and 3-dimension (3D) curves have been executed. Then, the hyperbolic curve-based evaluations have been presented for realizing the allowable variations of the Lyapunov coefficients focused on approaching zero inductors' current errors. Finally, a lab prototype model of the SIDO-TLC converter has been implemented. The proposed control technique has been verified through the experimental results in both steady and dynamic states. The experimental results confirmed the robustness and accuracy of the proposed controller in the presence of changes in the load and output voltages' references.

## References


[1] P. J. d. S. Neto, T. A. d. S. Barros, J. P. C. Silveira, E. R. Filho J. C. Vasquez, and J. M. Guerrero, "Power management strategy based on virtual inertia for dc microgrids," IEEE Transactions on Power Electronics, vol. 35, no. 11, pp. 12 472–12 485, 2020.

[2] U. Vuyyuru, S. Maiti, and C. Chakraborty, "Active power flow control between dc microgrids," IEEE Transactions on Smart Grid, vol. 10, no. 5, pp. 5712–5723, 2019.

[3] P. Prabhakaran and V. Agarwal, "Novel boost-sepic type interleaved dc–dc converter for mitigation of voltage imbalance in a low-voltage bipolar dc microgrid," IEEE Transactions on Industrial Electronics, vol. 67, no. 8, pp. 6494–6504, 2020.

[4] H. Shayeghi, S. Pourjafar, M. Maalandish, and S. Nouri, "Non-isolated DC–DC converter with a high-voltage conversion ratio," IET Power Electron., vol. 13, no. 16, pp. 3797–3806, 2020, DOI: 10.1049/iet-pel.2019.1014.

[5] H. Tian and Y. Li, "Virtual resistor based second-order ripple sharing control for distributed bidirectional dc–dc converters in hybrid ac–dc microgrid," IEEE Transactions on Power Electronics, vol. 36, no. 2, pp. 2258–2269, 2021.

[6] Z. Fan, B. Fan, W. Zhang, and W. Liu, "Distributed control of dc microgrids for optimal coordination of conventional and renewable generators," IEEE Transactions on Smart Grid, pp. 1–1, 2021.

[7] B. Wang, V. R. K. Kanamarlapudi, L. Xian, X. Peng, K. T. Tan, and P. L. So, "Model predictive voltage control for single–inductor multiple–output dc–dc converter with reduced cross regulation," IEEE Transactions on Industrial Electronics, vol. 63, no. 7, pp. 4187–4197, 2016.

[8] T. Chaudhury and D. Kastha, "A high gain multiport dc–dc converter fo integrating energy storage devices to dc microgrid," IEEE Transactions on Power Electronics, pp. 1–1, 2020.

[9] Z. Qian, O. Abdel-Rahman, and I. Batarseh, "An integrated four–port dc/dc converter for renewable energy applications," IEEE Transactions on Power Electronics, vol. 25, no. 7, pp. 1877–1887, 2010.

[10] Y. Li, X. Ruan, D. Yang, F. Liu, and C. K. Tse, "Synthesis of multipleinput dc/dc converters," IEEE Transactions on Power Electronics, vol. 25, no. 9, pp. 2372–2385, 2010.

[11] A. Farakhor, M. Abapour, and M. Sabahi, "Design, analysis, and implementation of a multiport dc–dc converter for renewable energy applications," IET Power Electronics, vol. 12, no. 3, pp. 465–475, 2019.

[12] Q. Tian, G. Zhou, M. Leng, G. Xu, and X. Fan, "A non–isolated symmetric bipolar output four–port converter interfacing pv–battery system," IEEE Transactions on Power Electronics, pp. 1–1, 2020.

[13] O. Ray, A. P. Josyula, S. Mishra, and A. Joshi, "Integrated dual–output converter," IEEE Transactions on Industrial Electronics, vol. 62, no. 1, pp. 371–382, 2015.

[14] E. C. dos Santos, "Dual–output dc–dc buck converters with bidirectional and unidirectional characteristics," IET Power Electronics, vol. 6, no. 5, pp. 999–1009, 2013.

[15] S. Markkassery, A. Saradagi, A. D. Mahindrakar, L. N, and R. Pasumarthy, "Modelling, design and control of non-isolated single–input multi–output zeta–buck–boost converter," IEEE Transactions on Industry Applications, pp. 1–1, 2020.

[16] Y. Chen and Y. Kang, "A fully regulated dual–output dc–dc converter with special-connected two transformers (sctts) cell and complementary pulsewidth modulation–pfm (cpwm–pfm)," IEEE Transactions on Power Electronics, vol. 25, no. 5, pp. 1296–1309, 2010.

[17] T. Chaudhury and D. Kastha, "A high gain multiport dc–dc converter for integrating energy storage devices to dc microgrid," IEEE Transactions on Power Electronics, pp. 1–1, 2020.

[18] G. Chen, Y. Liu, X. Qing, and F. Wang, "Synthesis of integrated multiport dc–dc converters with reduced switches," IEEE Transactions on Industrial Electronics, vol. 67, no. 6, pp. 4536–4546, 2020.

[19] J. Kim, S. Choi, and G. Moon, "Zero–voltage switching post regulation scheme for multioutput forward converter with synchronous switches," IEEE Transactions on Industrial Electronics, vol. 58, no. 6, pp. 2378–2386, 2011.

[20] K. Fujii, P. Koellensperger, and R. W. De Doncker, "Characterization and comparison of high blocking voltage igbts and iegts under hard– and soft–switching conditions," IEEE Transactions on Power Electronics, vol. 23, no. 1, pp. 172–179, 2008.

[21] L. F. Costa, S. A. Mussa, and I. Barbi, "Multilevel buck/boost-type dc–dc converter for high–power and high–voltage application," IEEE Transactions on Industry Applications, vol. 50, no. 6, pp. 3931–3942, 2014.
[22] K. Fujii, P. Koellensperger, and R. W. De Doncker, "Characterization and comparison of high blocking voltage igbts and iegts under hardand soft-switching conditions," IEEE Transactions on Power Electronics, vol. 23, no. 1, pp. 172–179, 2008.
[23] A. Ganjavi, H. Ghoreishy, and A. A. Ahmad, "A novel single–input dual–output three–level dc–dc converter," IEEE Transactions on Industrial Electronics, vol. 65, no. 10, pp. 8101–8111, 2018.
[24] X. Ruan, B. Li, Q. Chen, S.-C. Tan, and C. K. Tse, "Fundamental considerations of three-level dc–dc converters: Topologies, analyses, and control," IEEE Transactions on Circuits and Systems I: Regular Papers, vol. 55, no. 11, pp. 3733–3743, 2008.
[25] A. Ganjavi, H. Ghoreishy, A. A. Ahmad, and Z. Zhagn, "A three–level three–port bidirectional dc–dc converter," in 2018 IEEE International Power Electronics and Application Conference and Exposition (PEAC), 2018, pp. 1–4.
[26] Ganjavi, A., Gholinejad, H.R., Mehrasa, M., Gh oreishy, H. and Ahmad, A.A., 2020. Feedback–feedforward control technique with a comprehensive mathematical analysis for single-input dual-output three-level dc–dc converter. IET Power Electronics, 13(19), pp.4685-4694.
[27] S. Debnath, P. R. V. Marthi, Q. Xia, J. Pan, M. Saeedifard, V. N. Vipin, S. Chakraborty, and M. Arifujjaman, "Renewable integration in hybrid ac/dc systems using a multi-port autonomous reconfigurable solar powerplant (mars) IEEE Transactions on Power Systems, vol. 36, no. 1, pp. 603–612, 2021.
[28] V. Repecho, J. M. Olm, R. Grin˜o, A. Doria-Cerezo, and E. Fossas, "Modelling and nonlinear control of a magnetically coupled multiport dc-dc converter for automotive applications," IEEE Access, vol. 9, pp. 63 345–63 355, 2021.
[29] N. Mukherjee and D. Strickland, "Control of cascaded dc–dc converterbased hybrid battery energy storage systems—part ii: Lyapunov approach," IEEE Transactions on Industrial Electronics, vol. 63, no. 5, pp. 3050–3059, 2016.
[30] A. Lekic, D. Stipanovi ´ c, and N. Petrovi ´ c, "Controlling the ´ Cuk converter ´ using polytopic lyapunov functions," IEEE Transactions on Circuits and Systems II: Express Briefs, vol. 65, no. 11, pp. 1678–1682, 2018.
[31] J. M. Olm, E. Fossas, V. Repecho, A. Doria-Cerezo, and R. Garino ´"Adaptive control-based voltage regulation of a magnetically coupled multiport dc-dc converter for electrified vehicles applications," in 2020 IEEE International Symposium on Circuits and Systems (ISCAS), 2020, pp. 1–5.
[32] W. Tang and P. Daoutidis, "A bilevel programming approach to the convergence analysis of control-lyapunov functions," IEEE Transactions on Automatic Control, vol. 64, no. 10, pp. 4174–4179, 2019.

**Milad Rasouli** received the B.sc. and M.sc. degrees in electrical engineering from Babol Noshirvani University of Technology, Babol, Iran, In 2014 and 2017, respectively. He is currently working toward the Ph.D. degree in the Department of electrical engineering at the Lakehead University. His research interests include the control strategy of power converters and their applications in renewable energy and electric vehicles.

**Majid Mehrasa** (Member, IEEE) received the B.Sc. and M.Sc. degrees from the University of Mazandaran, Babol, Iran, in 2006 and 2009, respectively, and the Ph.D. degree from the University of Beira Interior (UBI), Portugal in 2019, all in electrical engineering. Then, He joined the University of Trieste, Italy and the University of Grenoble, Alpes, G2Elab, France as a Research Fellow and Postdoc Researcher in 2020 and 2021, respectively. In August 2022, he started a Post Doc Research Associate position at the Energy & Environmental Research Center (EERC) at the University of North Dakota (UND), Grand Forks, USA.

Dr. Mehrasa has authored over 100 publications as refereed journal articles, high-quality conference papers, and book chapter. His research interests include the multi-objective Design and Control of Power Electronic Converters (PECs), PECs Applications in HVdc, Microgrids, VSG, Smartgrids and Power Systems, Smart Charging/Discharging Strategies for Vehicle-to-Grid (V2G) applications, and Deep/Machine Learning Applications in PECs Control, V2G Systems and Power Systems.

**Amir Ganjavi (Member, IEEE)** received the B.Sc. and M.Sc. degrees in electrical engineering from Babol Noshirvani University of Technology, Mazandaran, Iran, in 2014 and 2017, respectively. He received his Ph.D. degree in electrical engineering with The University of Queensland (UQ), Brisbane, QLD, Australia. Since starting his Ph.D. program, he has worked as a doctoral researcher with Danfoss Drives A/S, Denmark. Recently, he has joined Queensland University of Technology (QUT) as a Research Fellow. During his research fellowship at QUT, he has been working on different projects, including DC microgrid design for green hydrogen production. His research interests include power converters and their applications in renewable energy, DC microgrids, control system design, electromagnetic interference (EMI), and power quality.

**Mahdieh S. Sadabadi** is currently Assistant Professor with School of Electronic Engineering and Computer Science, Queen Mary University of London, London, UK. Before that, she was an Assistant Professor with the Department of Automatic Control and Systems Engineering, University of Sheffield, United Kingdom. In addition, she was a Research Associate at the Department of Engineering, the University of Cambridge, and affiliated with Trinity College in Cambridge. Her research interests are generally centered on robust fixed-structure control of large-scale uncertain systems and resilient control systems with applications in power grids, microgrids, and power electronics converters.

**Hoda Ghoreishy** received the Ph.D. degree, specializing in power electronics and motor drives, from Tarbiat Modares University, Tehran, in 2012, all in electrical engineering. Her main research interests include the modeling, analysis, design, and control of power electronic converters/systems and motor drives. Her area of interest also includes embedded software development for power electronics and electric drives using microcontrollers and DSPs.

**Ahmad Ale Ahmad** was born in Babol, Iran, on August 6, 1980. He received the B.S., M.S., and Ph.D. degrees in electrical engineering from the Iran University of Science and Technology, Tehran, Iran, in 2002, 2006, and 2012, respectively. He served as a Researcher with the Iranian Research Institute of Electrical Engineering from 2002 to 2013, designing mediumand high-power converter. He is currently with the Department of Electrical Engineering, Babol Noshirvani University of Technology, Babol, Iran. His activities are currently focused on analog integrated circuit and power electronics.